New Journal and we have not received input yet 28 (2022) 101141

Contents lists available at ScienceDirect

Thermal Science and Engineering Progress

journal homepage: www.elsevier.com/locate/tsep

Top-down model of calcium carbonate scale formation in turbulent pipe flows

L. Moriconi [a,*], T. Nascimento [b], B.G.B. de Souza [b], J.B.R. Loureiro [b]

[a] Instituto de Física, Universidade Federal do Rio de Janeiro, C.P. 68528, CEP: 21941-972, Rio de Janeiro, RJ, Brazil
[b] Programa de Engenharia Mecânica, Coordenação dos Programas de Pós-Graduação em Engenharia, Universidade Federal do Rio de Janeiro, C.P. 68503, CEP: 21941-972, Rio de Janeiro, RJ, Brazil

ARTICLE INFO

Keywords:
Calcium carbonate scale formation
Particle laden flows
Turbulent pipe flows
Turbophoresis

ABSTRACT

We investigate calcium carbonate scale formation at high Reynolds numbers in a large pipe rig facility. The calcium carbonate solution is produced from the injection, at a T-joint inlet, of pH-stabilized sodium carbonate and calcium chloride aqueous solutions. A scanning electron microscopy analysis of the deposited mass along the pipe indicates that after an initial transient regime of ion-by-ion crystal growth, calcium carbonate scale is dominated by particulate deposition. While limescale formation in regions that are closer to the pipe's entrance can be described as the heterogeneous surface nucleation of calcium and carbonate ions driven by turbulent diffusion, we rely upon turbophoresis phenomenology to devise a peculiarly simple kinetic model of deposition at farther downstream regions. Letting Φ and R be the flow rate and the pipe's radius, respectively, the mass deposition rates per unit time and unit area are predicted to scale as Φ^{α}/R^{β} (for certain modeled values of the α and β parameters) with suggestive support from our experiments.

1. Introduction

The spontaneous formation of calcium carbonate ($CaCO_3$) scale, also known as limescale, is an ordinary phenomenon long known to affect the efficiency of water supply networks, boilers and heat exchangers [1,2]. Limescale formation is also a great source of worry in the oil industry, where it leads, from time to time, to operational issues that are commonly found from the deep production pipelines installed in oil reservoir cores up to topside facilities [3–5]. Particularly dramatic instances of calcium carbonate scale are those related to the exploration of carbonate reservoirs, which actually hold about 60% of all of the world oil reserves [6].

Stated in the most synthetic way, calcium carbonate molecules are produced from the binding of calcium and carbonate ions in aqueous solution [1], as represented by the following chemical reaction,

$$H_2O + CO_2 + CaCO_3 \leftrightarrow Ca^{2+} + 2HCO_3^-.$$

Pressure, temperature or ion concentration variations that come along the lifetime of an oil production setup, for instance, eventually drive the above reaction to the left, when the calcium carbonate solution becomes supersaturated and breaks the thermodynamic equilibrium of the once-untouched oil reservoir. Limescale can then grow by heterogeneous nucleation of ions at surfaces or by the deposition of bulk pre-existent (nucleated or aggregated) calcium carbonate particles. It is, actually, a matter of great interest to understand under what conditions limescale develops through ion-by-ion growth or particulate deposition [7,8].

The immense global budgets applied to the mitigation of calcium carbonate scale formation in all of its manifestations are not associated, as a rule, to environment-friendly procedures, to the extent that they are tied to the use of pollutant chemical additives. It is worth mentioning, nevertheless, that remarkable efforts have been done to devise green chemical agents and the implementation of alternative clean anti-scale methods, as the ones based on the use of ultrasound or electromagnetic devices [9–11]. In this connection, it is almost unnecessary to emphasize that progress in the understanding of the physical–chemical basis of limescale formation has a strong potential for innovations of wide social relevance.

Even though the detailed out-of-equilibrium dynamics of calcium carbonate nucleation is still barely understood [12–15], its metastable/stable phases can be addressed through thermodynamic modeling or customized experiments [16,17]. It is also viable to investigate the formation of limescale (in the presence or absence of chemical additives) in capillary tubes, with pressures, temperatures, and solution samples which emulate the ones unveiled in realistic situations [18].

A natural difficulty in weighting the relevance of thermodynamic modeling and the performance of capillary flow experiments comes

* Corresponding author.
E-mail address: moriconi@if.ufrj.br (L. Moriconi).

https://doi.org/10.1016/j.tsep.2021.101141
Received 25 August 2021; Received in revised form 10 November 2021; Accepted 11 November 2021
Available online 26 November 2021

from the fact that in the real world the production of calcium carbonate scale does not develop, usually, under quasi-static conditions. Turbulence with a variety of boundary conditions and/or sudden variations of thermodynamic parameters provide, actually, the general stage where deposited limescale is observed.

In the present study, we avoid thermodynamic and chemical complications, restricting our work to supersaturated calcium carbonate aqueous solutions. We focus on the phenomenon of limescale formation in turbulent pipe flows, as realized in experiments performed under ambient temperatures and outlet atmospheric pressure. In order to model the mass deposition rate along the pipe, we take the standpoint, to be concluded from scanning electron microscopy (SEM) images, that the dominant mechanisms of scale formation change along the pipe, ranging from ion crystallization, for some extension after the inlet, to the deposition of calcium carbonate particles at farther downstream regions.

Having in mind the enormous complexity of limescale formation under turbulent conditions, related to the coupling of hydrodynamic and chemical phenomena over a broad range of length scales, we rely on a much simpler top-down modeling strategy. A reduced number of hypotheses are put forward, which take into account elementary known facts about near-wall particle-laden flows, combined with feedback experimental inputs.

This paper is organized as follows. The experimental setup, the experiment preparation and its measurement protocols are detailed in Section 2. Next, in Section 3, we collect empirical information associated to the observed limescale formation in the pipe flow experiments and devise, accordingly, elementary models for the prediction of mass deposition rates. We work upon qualitative hints derived from SEM images (Hitachi Tabletop Microscope TM3030), pressure drop measurements and particle size distributions (Malvern Panalytical Mastersizer 3000) taken along the flow. Closer to the inlet region, calcium carbonate deposition is modeled as a turbulent diffusive process of calcium and carbonate ions in the vicinity of the pipe's inner surface. For the far downstream regions, on the other hand, we resort to the phenomenology of turbophoresis phenomena [19–24] to introduce a system of coupled time evolution equations for the bulk mass densities of two classes of particles, which are characterized by their local Stokes numbers defined in the inner boundary layer region. An appendix provides estimates for the sizes of the calcium carbonate particles that are likely to be captured by the pipe's inner surface, due to attractive van der Waals interactions.

In Section 4, we report mass deposition rate measurements and discuss them under the light of the present modeling framework. Finally, in Section 5, we summarize our findings and point out directions of further research.

2. Experimental setup and procedures

Three reservoirs which are open to the atmosphere (at sea level), with volumes in the range of 1.0–7.5 m^3, were used to store pH neutral potable water and aqueous solutions of calcium chloride ($CaCl_2$) and sodium bicarbonate ($NaHCO_3$). As a purification protocol, particles with linear sizes smaller than 5 μm were removed from the fluid, through the use of carbon activated filters.

As a fundamental procedure to ensure test reproducibility, the aqueous ionic solutions were stirred for about 5 days until their carbon dioxide vapor pressures and pHs reached stable equilibrium values. Only after this preparation step, the turbulent pipe flow was started for the investigation of limescale formation. Table 1 summarizes the physical–chemical properties of the aqueous solutions before they were injected into the pipe.

The ionic solutions were simultaneously pumped through a T-joint inlet (with identical flow rates) into a 70 m long acrylic pipe with inner diameter D of 11 mm. At operating pressures in the range of 1–10 bars and environmental temperatures around 300 K, our mixed ionic solutions turned out to be supersaturated (by a far amount) for the precipitation of calcium carbonate particles. The exit flow was directed to a discharge reservoir open to the atmosphere. The essential schematics of the experiment is depicted in Fig. 1.

Table 1
Physical–Chemical characterization of the aqueous ionic solutions.

Aqueous Solution of	$CaCl_2$	$NaHCO_3$
Concentration (g/l)	7.35 ± 0.05	12.6 ± 0.05
Conductivity (mS/cm)	9.73 ± 0.59	10.80 ± 0.38
pH	7.48 ± 0.31	9.02 ± 0.26

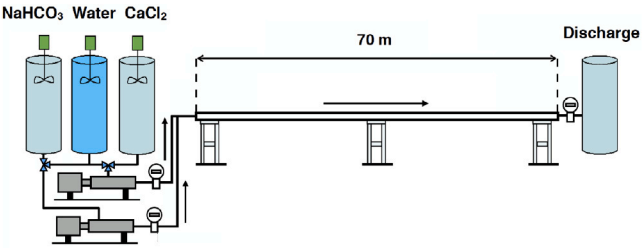

Fig. 1. A layout of the experimental setup.

With the help of three-way valves, the reservoirs that contain calcium chloride and sodium bicarbonate reservoirs were kept initially closed, so that the water reservoir could be used to establish a turbulent pipe flow free of air bubbles. When this is accomplished, the water reservoir is closed and the ionic solutions are pumped into the pipe, without variations of the total flow rate. A fifth reservoir (not shown in Fig. 1) which stores an aqueous solution of acetic acid (10% v/v) is employed to clean the pipe from the limescale that remains attached to it at the end of the tests.

As sketched in Fig. 1, two electromagnetic flow meters (Incontrol VMS PRO) were inserted in parallel lines in front of the pipe's inlet in order to set equal flow rates for the fluids that were pumped from different reservoirs. Right after the pipe's outlet, a Coriolis flow meter (Endress+Hauser Promass 83F) was placed there to provide a redundant measurement of the total pipe's flow rate.

Several pressure taps and points for fluid sampling (for the sake of particle size distribution analyses) were equally spaced along the pipe. In addition, the pipe had twelve 14 cm lengthwise test sections, distant from each other by approximately 6 m, that could be removed (and reattached) for measurements of the deposited calcium carbonate mass and for the scrutiny of scanning electron microscopy.

The viscosity of the very dilute solutions of ions and suspended particles was identified, in practice, to the one of water. We have studied limescale formation for five flow rates given by $\Phi = 300, 450, 600, 750,$ and 1000 l/h, corresponding, approximately, to the Reynolds number range $10^4 < \mathrm{Re} < 3 \times 10^4$ (friction Reynolds numbers in the interval $300 < \mathrm{R}_\tau < 800$).

3. Deposition model

We address here a number of phenomenological aspects of limescale formation, which are particularly related to our experiments and constitute the basic ingredients for the modeling considerations carried on in this work.

It is important to stress, as a remark of methodological nature, that the data we have collected was not primarily aimed to support any pre-established model of ion/particulate deposition. The results of the experimental campaign reported below, rather, were intended to provide characterization data, i.e., empirical pieces of information "in search" of a theoretical framework.

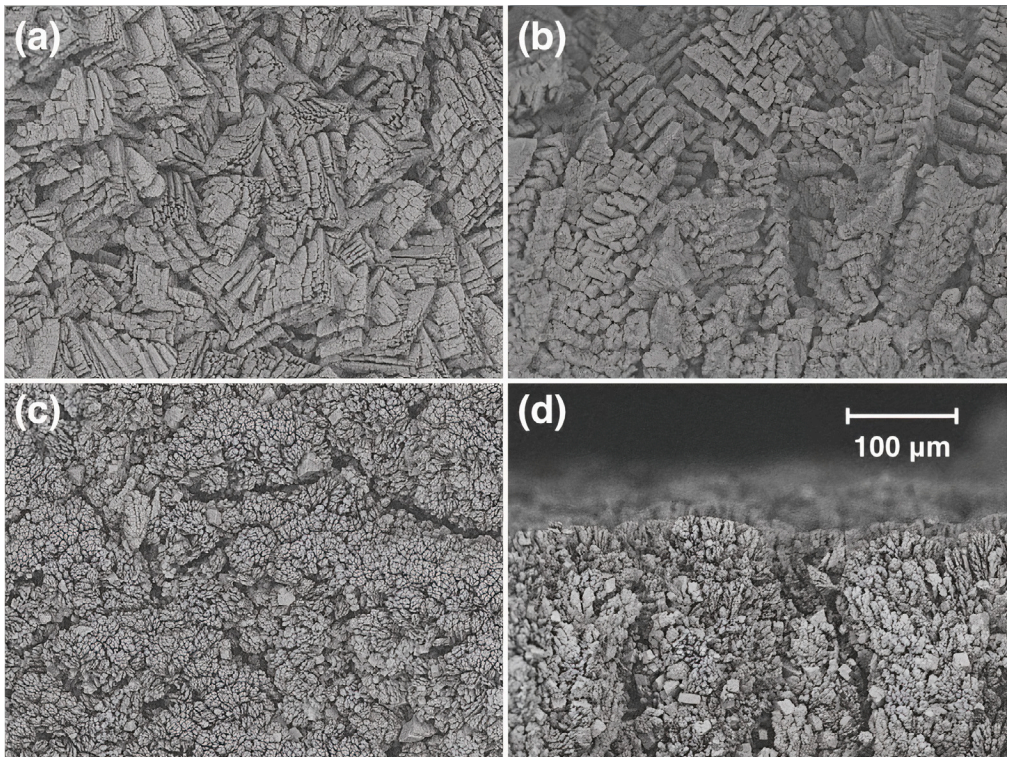

Fig. 2. SEM images of calcium carbonate scale in a turbulent pipe flow.

3.1. The nature of the deposition process

Limescale formation is expected to occur, in principle, through heterogeneous surface nucleation (ion-by-ion interface growth) and/or by the deposition of calcium carbonate colloidal particles which have sizes of a few micrometers. Very small (nanometer-sized) particles, initially created through nucleation in the bulk flow, can subsequently grow by ion accretion or form larger particles through aggregation.

To resolve the issue of what are the specific scale processes that took place in our experiments, we have inspected SEM images of the limescale produced in different positions along the pipe.

Fig. 2 shows SEM images for one of the turbulent runs (Φ = 1000 l/h, Re $\simeq 3 \times 10^4$) taken after 105 mins from the experiment start. In Figs. 2a and 2c, we report SEM top view images; side view images are given in Figs. 2b and 2d. All the four pictures have the same scale as the one indicated in Fig. 2d. The snapshot pairs (2a, 2b) and (2c, 2d) were taken, respectively at circa 2 and 65 meters away from the pipe's inlet. As it is suggested from Figs. 2a and 2b, limescale formation is characterized, near the inlet, by the piling and juxtaposition of several broken crystalline pieces of calcium carbonate. Following standard ideas of crystal growth theory [25], the stacked crystal facets and the pyramidal structures visualized in the referred images can be taken together as a strong indication that limescale grows near the pipe's inlet through ion-by-ion deposition. Far from the inlet, images (2c) and (2d), the granular structure of limescale suggests that it grows mainly by particulate deposition.

Farther downstream, in fact, faceted small crystal pieces of calcium carbonate are much less frequently observed, and limescale turns out to be dominated by the aggregation of small-sized (<10 μm) particles, which form clusters that closely resemble the ones produced in diffusion limited aggregation processes [26].

3.2. Limescale roughness

As it will be clarified in Sections 3.3 and 3.4, a point of particular importance in our modeling definitions is the correct assessment of roughness effects on mass deposition rates. Roughness can be usually quantified with the help of Moody charts [27], once the friction factor f and the Reynolds number Re are known. The friction factor is defined, as usual, from the relation [27,28]

$$\frac{dP}{dx} = f \frac{\rho_f}{2} \frac{v^2}{D^3} \mathrm{Re}^2 \,, \tag{3.1}$$

for the pressure gradient dP/dx, where x is the axial coordinate along the pipe. Above, ρ_f and v are the fluid density and the fluid kinematic viscosity, respectively.

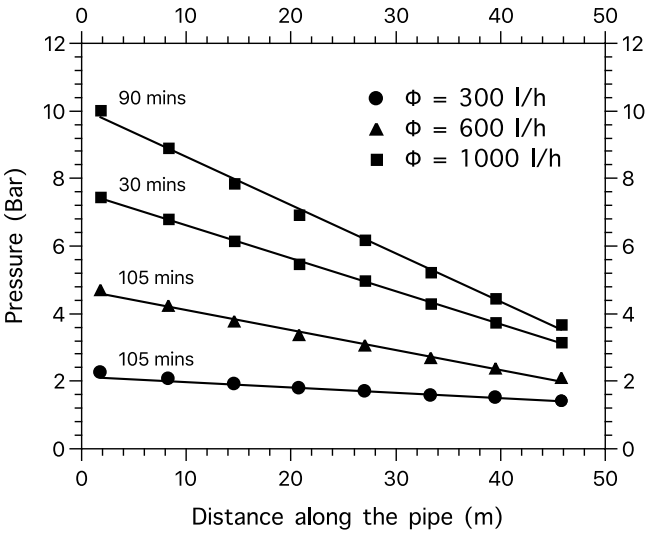

Fig. 3. A sample of pressure measurements taken along the pipe.

Pressure measurements were performed along the pipe in all of the experiments, up to a distance of around 45 meters away from the pipe's inlet. Fig. 3 reports a representative sample of data. Pressure gradients

are approximately constant in space, but their absolute values grow in time as it is pointed out from the data collected at different times (30 mins and 90 mins), for the highest Reynolds number case. Roughness growth is, in fact, a well-known phenomenon generally associated to the kinematics of evolving interfaces [29].

It turns out, from the evaluation of pressure gradients at different times and the use of Eq. (3.1), that the friction factor evolves, within the time scale of 90 mins after the flow starts, up to $f \simeq 4.0 \times 10^{-2}$, regardless the Reynolds number. We have checked that this estimate is not meaningfully affected if the pressure of 1 bar at 70 meters (the pipe's outlet) is added as a common measurement point to all the four datasets in Fig. 3.

A quick look at a Moody chart tells us, on the other hand, that by taking $f \simeq 4.0 \times 10^{-2}$ at $\mathrm{Re} = 10^4$, the friction factor should drop by around 10% as the Reynolds number increases along the explored range, if the relative pipe roughness were fixed. This means that the pipe relative roughness in our experiments gets larger, for some prescribed evolution time of limescale formation, the larger is the Reynolds number. As a combination of two roughly canceling effects, thus, the friction factor f is approximately Reynolds number independent.

Of course, our considerations about limescale roughness are based on comparisons between the empirical friction factors obtained from our particular pipe flow experiments and the ones established for the special classes of rough surfaces compiled in the Moody chart. We have to keep in mind that roughness parameters inferred from friction factors are always dependent on both the dynamical and geometrical aspects of the flow. It may be difficult, thus, to disentangle their combined roles in the values of pressure gradients, an issue which we leave as an interesting subject for additional studies.

3.3. Limescale formation by ion deposition

Near the pipe's inlet, calcium and carbonate ions are transported to the wall by turbulent diffusion. The rate of mass deposition (mass deposited per unit time and unit area) $\dot{\sigma}$ can be written as

$$\dot{\sigma} \propto D_* \frac{\delta c}{\ell} \ , \tag{3.2}$$

where $D_* \propto \ell v_*$ is the turbulent diffusion coefficient and ℓ and v_* are the boundary layer scales of length (viscous length) and velocity (friction velocity), respectively [28]. Above, the ion concentration gradient is estimated as $\delta c/\ell$, where δc is the ion concentration variation across the viscous sublayer. Eq. (3.2) is, actually, an application of the "gradient diffusion" model of deposition within viscous length scales [19,20].

Let $\boldsymbol{\Phi}$ and R be, respectively, the flow rate and the pipe's radius. Taking δc to be flow rate independent (which is a reasonable assumption for the pipe's inlet region), we find, from (3.2),

$$\dot{\sigma} \propto v_* = \frac{v_*}{U} U \propto \sqrt{f}\, \frac{\boldsymbol{\Phi}}{R^2} \propto \frac{\boldsymbol{\Phi}}{R^2} \ , \tag{3.3}$$

where we have evoked the usual relationship between the dimensionless ratio v_*/U and the friction factor f [28],

$$f = 8 \left(\frac{v_*}{U} \right)^2 \ , \tag{3.4}$$

and the fact that f is Reynolds number independent in our pipe flow experiments.

3.4. Limescale formation and turbophoresis

Limescale formation due to particulate deposition, assumed to take place in farther downstream positions along the pipe, requires modeling ideas which are a way more complex than the ones associated to ion-by-ion deposition driven by turbulent diffusion. To start, let us investigate whether significant contributions to deposition may occur through the transport of calcium carbonate particles that behave as tracers.

Since electrostatic or van der Waals interactions have to overcome particle drag forces for deposition to occur, tracer particles will be deposited only if they get close to the walls within atomic length scales (see the discussion carried out in the Appendix). Turbulent diffusion, which should play here a role similar to the one previously addressed for the regime of ion-by-ion deposition, could be conjectured to be the main mechanism for the particulate deposition snapshotted in Figs. 2c and 2d. This is, however, an unlikely scenario.

While we expect to have many more tracer (smaller) particles near the pipe's inlet than elsewhere, no relevant signature of particulate deposition is found in that region, as already concluded from the inspection of Figs. 2a and 2b. We find, actually, that near the pipe's inlet the vast majority of particles have their sizes peaked around 10 μm, as noticed from the particle volume distributions provided in Figs. 4a and 4b. Particle size measurements were taken near the pipe's inlet (at distances of 2 m away from it; black solid lines in Figs. 4a and 4b) and far from the pipe's inlet (at distances of 68 m away from it; red dotted lines in Figs. 4a and 4b), after the first 30 mins of deposition, for the flow rates of $\boldsymbol{\Phi} = 300$ l/h (Fig. 4a) and $\boldsymbol{\Phi} = 1000$ l/h (Fig. 4b). In short, we address henceforth the point that particulate deposition was produced in our experiments through the collisions of larger, inertial particles, with the pipe's inner surface.

It is interesting to digress a bit on the procedure carried out for the determination of the relative volume distributions depicted in Figs. 4a and 4b. The measurement device (Malvern Mastersize 1300) was initially cleaned and calibrated with purified water (from the same source as the one which fed the ionic solutions in the reservoirs) to specifically operate with calcium carbonate particles. In order to collect saturated bulk fluid samples of 500 ml and immediately transfer them to the analyser, the turbulent pipe flow is momentarily stopped. The distributions here reported result from averaging over three independent evaluations taken for the same samples. The size of measurement bins are not fixed, being about 10% of the particle's measured size. We have removed, from Figs. 4a and 4b, negligible contributions given by very small particles, which have sizes that typically range from 0.5 μm to 5.0 μm (if numerous enough, the analyser's would be able, in principle, to produce statistical data for particles with sizes larger than about 10 nm).

Once tracers are ruled out as actors of particulate deposition, the phenomenon of turbophoresis [19–24] comes to mind as soon as we center our attention on the dynamics of inertial particles. In the case of turbulent pipe flows, inertial particles are known to concentrate preferably close to the walls, up to the top of the buffer layer [23]. It is imperative to devise, thus, estimates of the local Stokes number,

$$\mathrm{St}^+ \equiv \frac{1}{18} \frac{\rho_p}{\rho_f} \frac{d^2 v_*^2}{\nu^2} \ , \tag{3.5}$$

for the transported particles, in order to evaluate their roles in the deposition process. Above, ρ_p and d are, respectively, the particle's mass density and its diameter. We note that $\mathrm{St}^+ \propto (d^2/\nu)/(\ell/v_*)$, that is, the above Stokes number is just the ratio of the relaxation time scale derived from the Stokes flow around a particle, d^2/ν, to the viscous time scale at the turbulent boundary layer, $\ell/v_* = \nu/v_*^2$.

Following the quantitative results established in Picano et al. [23] and Sardina et al. [24] on the distribution of transported particles in wall turbulence, we adopt the physical picture that particles which have Stokes numbers larger than $\mathrm{St}^+ \simeq 5$ are the ones which maximize their concentrations in the turbulent boundary layer region $y^+ < 30$, where y^+ is the distance to the wall represented in viscous length units, that is, $y^+ \equiv y/\ell$ [30]. The effective classification of particles as tracers or inertial can be actually put forward from the condition that they have, respectively, Stokes numbers smaller or larger than $\mathrm{St}^+ \simeq 5$. Using (3.5), we find that the weakly inertial particles with $\mathrm{St}^+ \simeq 5$ have linear sizes around 70 μm and 20 μm for the flow rate cases $\boldsymbol{\Phi} = 300$ l/h and $\boldsymbol{\Phi} = 1000$ l/h, respectively. Referring to Figs. 4a and 4b, we see that those numerical estimates for the sizes of the most

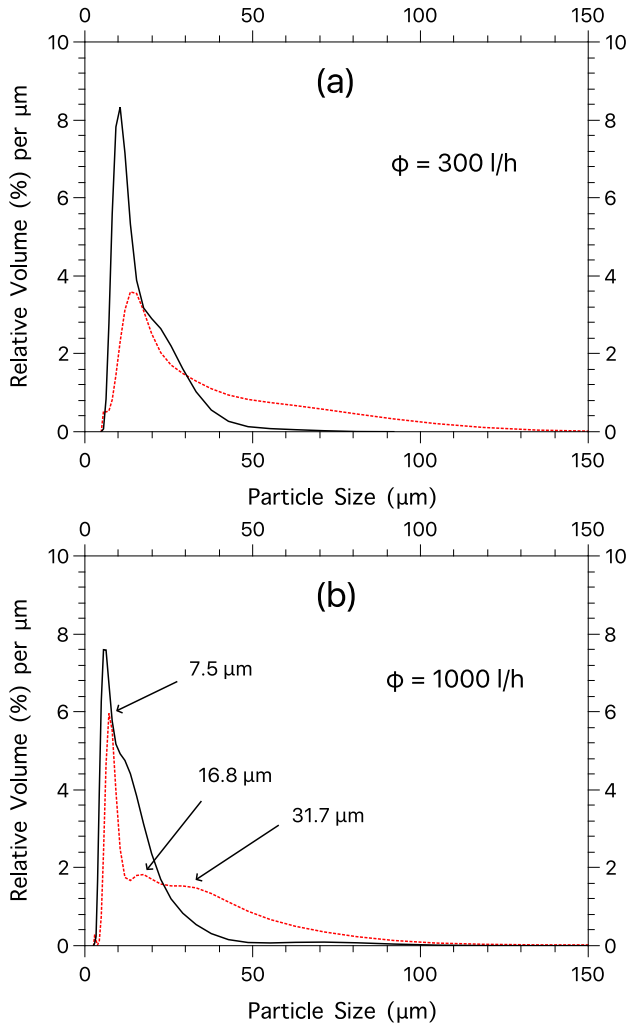

Fig. 4. Relative volume occupied by suspended particles per particle size variation.

concentrated turbophoretic inertial particles are consistent with our view that the deposition of tracers can be neglected in the process of limescale formation. Larger inertial particles are, furthermore, likely to be generated from the pair aggregation of smaller particles, as suggested from the relative volume peaks evidenced in Fig. 4b, which are roughly related to each other by powers of two. It should be noted that the secondary peaks of Fig. 4b are not present in the data of Fig. 4a. We do not have yet a clear understanding of this phenomenon, which seems to be very likely related to the intensification of particle aggregation kinetics at larger flow rates.

It is puzzling, however, that while we expect particles with linear sizes larger or of the order of 20 μm to be the right candidates for particulate deposition in the flow rate case $\Phi = 1000$ l/h, we find, from Figs. 2c and 2d, that the deposited particles have sizes no larger than 10 μm. A possible solution of this issue may rely on the hypothesis that particles which collide with the depositing surface are broken up into a number of smaller particles. This is, actually, what happens in the deposition of supercooled large droplets on the surface of airplane wings [31], a largely studied icing phenomenon, relevant for the sake of aircraft flight safety.

Raising a bridge from the problem of icing on wings to the one of limescale formation in pipe flows is an interesting perspective, whose investigation goes far beyond our present scopes. The main motivation to pursue this goal would be the close analogy that there is

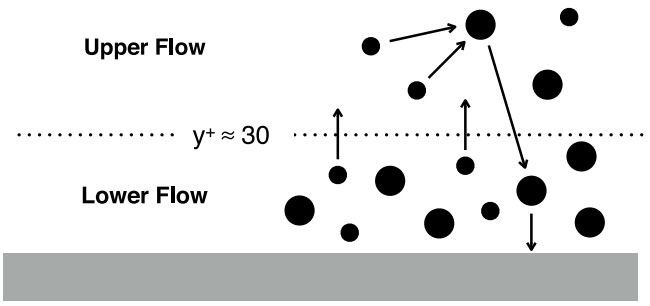

Fig. 5. Schematic distribution of S and L-particles within turbulent boundary layer scales.

between supercooled large droplets of water below the freezing point and metastable calcium carbonate particles in supersaturated solutions.

Reaction–Advection Model of Particulate Deposition

We aim at introducing a model as elementary as possible, in order to account for limescale formation due to particulate deposition in our pipe flow experiments. To begin with, we classify the inertial calcium carbonate particles in the flow into two broad size classes. They are labeled as the classes of "small" (S) and "large" (L) particles, operationally defined from the conditions that

(i) L-particles are the ones which are produced from the aggregation of S-particles

and that

(ii) S and L-particles have Stokes numbers larger than $St^+ \simeq 5$, the threshold for enhanced particle concentration in the boundary layer range $y^+ < 30$, as suggested from turbophoresis phenomenology.

It is not difficult to show, using (3.5) and mass conservation, that a more quantitative definition of these particle classes can be equivalently given by requiring S and L-particles to have, respectively, Stokes numbers in the ranges $5 \leq St^+ \leq 5 \times 2^{2/3} \simeq 8$ and $St^+ > 8$. These estimates may be subject to further revision, which, however, we do not expect to change our main results, as evidenced from the subsequent arguments.

Let, in self-evident notation, ρ_s and ρ_l be the approximately homogeneous bulk mass densities associated to these two particle classes, at distances $y^+ > 30$ away from the deposition surface. We assume that most of particulate deposition comes from collisions of the more massive L-particles with the pipe walls. The mass deposition rate can then be put forward here as

$$\dot{\sigma} = \kappa_l \rho_l v_* \ , \tag{3.6}$$

where κ_l is a dimensionless transport constant and we have taken the friction velocity v_* as the natural velocity scale for surface deposition.

If particles did not interact among themselves, we would expect, in the absence of deposition, to have a perfect balance of mass fluxes across the boundary of the turbophoretic region $y^+ < 30$, towards and from upper regions of the flow, for each one of the particle size classes [23]. However, particles not only aggregate but also break and deposit, so that the detailed balance of incoming and outcoming mass fluxes for both of S and L-particle classes breaks down in the boundary layer. At this point a few important remarks are in order:

R1. The measured mass deposition rates have been found to approach asymptotic stable values farther downstream from the pipe's inlet, where particulate deposition dominates;

R2. Particles are intermittently exchanged between the lower ($y^+ < 30$) and the upper ($y^+ > 30$) flow region, due to the drag provided by boundary layer ejections and sweeps (which are then also related to bursts of particle deposition) [21];

R3. Most of particle aggregation and breakup events are assumed to take place in the upper flow region, which contains the vast majority of particles.

Above, **R1** imposes a constraint that any conceivable model should comply with; remark **R2** implies that both the S and L-particle mass fluxes toward and from the upper flow region can be taken as proportional to $\rho_s v_*$ and $\rho_l v_*$, respectively; assumption **R3**, on its turn, indicates that variations of the bulk mass densities ρ_s and ρ_l associated to aggregation and breakup phenomena can be accounted entirely from balance equations devised for the upper flow domain.

We emphasize, additionally, that as far as L-particles dominate mass deposition, and both ρ_s and ρ_l are asymptotically constant at large distances from the pipe's inlet, in view of **R1**, breakup processes can be neglected *vis-à-vis* the role of S-particle aggregation in the production of bulk L-particles. It is clear, then, that asymptotic plateaus for ρ_s and ρ_l are only possible if the mass of S-particles that is lost in the bulk due to aggregation is compensated through a net flux of S-particles from the inner flow region (which acts like a particle reservoir).

This general physical picture of deposition is visually summarized in Fig. 5: due to turbophoresis [23], inertial particles tend to accumulate in a lower flow region roughly defined by $y^+ < 30$. S and L-particles are represented in Fig. 5 (of course, completely out of scale) as the smaller and larger filled circles, respectively. Particle populations are assumed to be constant in the upper flow, at the expenses of bulk aggregation and unbalanced particle exchanges with the lower flow region. The existence of non-canceling upward and downward particle fluxes for individual particle classes is ultimately associated to the phenomenon of particulate deposition.

Since our experiments were carried out for dilute particle suspensions, the mass density of L-particles is expected to increase, on the grounds of the binary aggregation of bulk S-particles, with rate $\gamma\rho_s^2$, where γ is some reaction constant. We can also model the net mass flux of S-particles (mass per unit area per unit time) from the lower to the upper flow region as $\kappa_s\rho_s v_*$, where κ_s is a dimensionless coefficient analogous to the one introduced in Eq. (3.6). It follows immediately that along a pipe's lengthwise section of extension Δ, the bulk mass of S-particles would increase with rate $2\pi R\Delta\kappa_s\rho_s v_*$, if aggregation/breakup effects were neglected. As a consequence, the mass density production rate for the bulk S-particles, neglecting again mass variations from aggregation or breakup processes, is estimated as $2\pi R\Delta\kappa_s\rho_s v_*/\pi R^2\Delta = 2\kappa_s\rho_s v_*/R$. In the same fashion, it turns out that the (negative) mass density production rate for the L-particles, if restricted to the process of mass transport to the lower flow region (and subsequent deposition) amounts to just $-2\kappa_l\rho_l v_*/R$.

Putting together the phenomenological points discussed so far, we propose to describe the space–time dependence of the bulk densities $\rho_s = \rho_s(x,t)$ and $\rho_l = \rho_l(x,t)$ along the pipe by means of the following minimalist pair of kinetic differential equations,

$$\frac{d\rho_s}{dt} = -\gamma\rho_s^2 + 2\frac{\kappa_s v_*}{R}\rho_s \ , \tag{3.7}$$

$$\frac{d\rho_l}{dt} = \gamma\rho_s^2 - 2\frac{\kappa_l v_*}{R}\rho_l \ , \tag{3.8}$$

where $d/dt = \partial_t + U\partial_x$ is the material derivative for a flow with (effective) advective bulk velocity U. Eqs. (3.7) and (3.8) can be interpreted as a reduced formulation of population balance dynamics [32] for the dispersed particulate phase. The one-dimensional model addressed here is supported by the fact that the density of transported particles can be separated into two approximately homogeneous classes, as indeed suggested from numerical simulations [23,24].

Far enough from the pipe's inlet, both $d\rho_s/dt$ and $d\rho_l/dt$ vanish, so that

$$\kappa_s\rho_s = \kappa_l\rho_l \ , \tag{3.9}$$

as it can be inferred from (3.7) and (3.8). Once most of the depositing mass is supposed to belong to the L-particle class, we have $\rho_l \gg \rho_s$. Eq. (3.9) leads, thus, to $\kappa_s \gg \kappa_l$. This latter inequality implies that ρ_s relax to its equilibrium value $\bar{\rho}_s$ much faster than ρ_l does. Taking $d\rho_s/dt = 0$ in Eq. (3.7) and solving for ρ_s, it follows that

$$\bar{\rho}_s = \frac{2\kappa_s v_*}{\gamma R} \ . \tag{3.10}$$

Replacing ρ_s in the first term of the right-hand side of (3.8) by (3.10), and working in the stationary regime where ρ_l becomes time-independent, Eq. (3.8) becomes

$$U\frac{d\rho_l}{dx} = \frac{4\kappa_s^2}{\gamma R^2}v_*^2 - \frac{2\kappa_l v_*}{R}\rho_l \ . \tag{3.11}$$

Eq. (3.11) can be straightforwardly solved to give

$$\rho_l(x) = \rho_0\exp\left(-\frac{2\kappa_l v_*}{RU}x\right) + \frac{2\kappa_s^2}{\gamma\kappa_l R}v_*\left[1-\exp\left(-\frac{2\kappa_l v_*}{RU}x\right)\right] \ , \tag{3.12}$$

where $\rho_0 = \rho_l(0)$ is the arbitrary initial condition for the density field $\rho_l(x)$.

It is interesting to express, again, the friction velocity v_* in Eq. (3.12) as a function of the friction factor f, Eq. (3.4). We also introduce in the modeling a friction factor exponent α which relates the friction factor to the Reynolds number, as

$$f \equiv f_0 Re^{-\alpha} = f_0\left(\frac{\pi R\nu}{2}\right)^{\alpha}\Phi^{-\alpha} \ . \tag{3.13}$$

In consonance with the discussion of Section 3B, we take $\alpha = 0$ in practice. Note, in passing, that the standard Blasius relation is given by (3.13) with $\alpha = 1/4$ [28].

Collecting Eqs. (3.4), (3.6), (3.12), and (3.13), the mass deposition rate may be written, now, as the position dependent function,

$$\dot{\sigma}(x) = a\exp\left(-b\Phi^{-\alpha/2}x\right) + c\Phi^{2-\alpha}\left[1-\exp\left(-b\Phi^{-\alpha/2}x\right)\right] \ , \tag{3.14}$$

where

$$a = \kappa_l\rho_0 v_* \ , \tag{3.15}$$

$$b = 4\sqrt{2f_0}\kappa_l\left(\frac{\pi\nu}{2}\right)^{\alpha/2}R^{\alpha/2-1} \ , \tag{3.16}$$

$$c = \frac{16}{\pi^2}\frac{\kappa_s^2}{\gamma}f_0\left(\frac{\pi\nu}{2}\right)^{\alpha}R^{\alpha-5} \ . \tag{3.17}$$

It could be pointed out that there is a somewhat large room for reasonable phenomenological fittings of mass deposition rates from the use of Eq. (3.14), since there are three independent unknown parameters in the model (a, b, and c). However, as argued in the next section, we develop, as a more restrictive test of the model's consistency, a systematic procedure of analysis which considerably reduces the freedom in the choice of fitting parameters.

4. Results

Our task now is to discuss the experimental validation of the modeling expressions (3.2) and (3.14) for the mass deposition rates. We start with the latter.

It is interesting to note that the b and c parameters in (3.16) and (3.17) do not explicitly depend on the flow rate Φ or on the initial density parameter ρ_0, as in (3.15). It is likely, thus, that b and c depend *only* on the chemical concentrations of calcium and carbonate ions (and of carbon dioxide, as well) injected into the pipe flow, which were approximately the same for all the investigated flow rate cases. Taking $d\rho_l/dx = 0$ in Eq. (3.11) or using Eq. (3.14), furthermore, we are led to the fact that for $\alpha = 0$ the mass deposition rate approaches, far from the pipe's inlet, the asymptotic value

$$\dot{\sigma}_\infty = c\Phi^2 \propto \frac{\Phi^2}{R^5} \ . \tag{4.1}$$

The above simple observations can be used to introduce a consistent strategy for the definition of the open phenomenological parameters in (3.14), as it follows. We consider, initially, one of the flow cases where mass deposition rates were measured with the smallest relative error bars, say, the one with $\Phi = 300$ l/h and get c straightforwardly from the mass deposition rate taken at the farthest measurement point downstream along the pipe. From the inspection of the several mass deposition rate curves, we also restrict to $x > 20$ m the range of positions where particulate deposition is supposed to dominate limescale

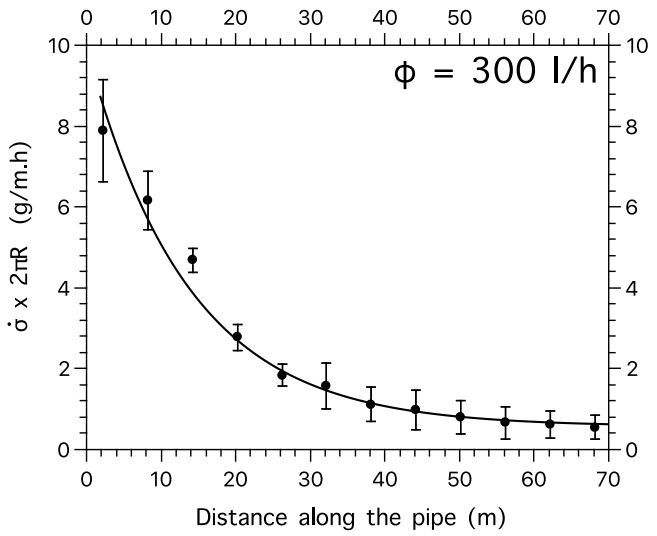

Fig. 6. Measured and modeled mass deposition rates for the flow rate case $\Phi = 300$ l/h.

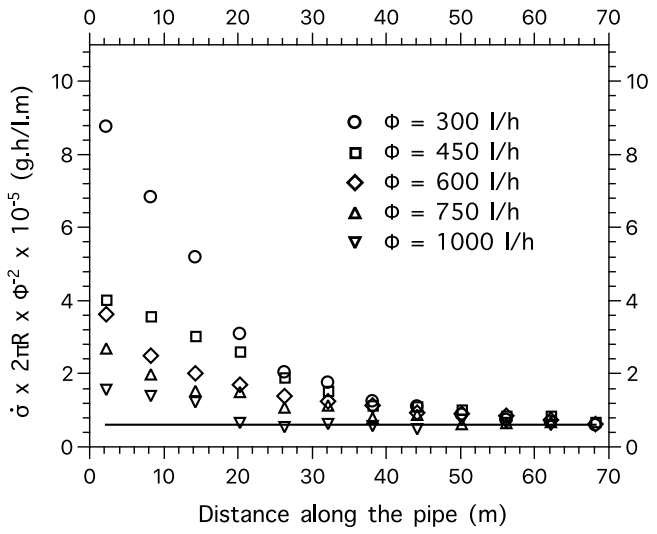

Fig. 7. Asymptotic data collapse for all of the measured mass deposition rates.

formation. The pair of additional parameters, a and b, are determined afterwards from optimizations based on the least square method, see Fig. 6.

The solid line in Fig. 6 is derived from Eq. (3.14), with $\alpha = 0$. The error bars associated to measurements are estimated from three independent experimental runs. We get $a \times 2\pi R = 10.0$ g/m·h, $b = 7.3 \times 10^{-2}$ m^{-1} and $c \times 2\pi R = 6.1 \times 10^{-6}$ g/m·h.

When dealing with other flow rate cases, b and c are not replaced by any other estimates. Optimal fittings are then established by adjustments of a, the only remaining free parameter in the application of Eq. (3.14) to further experimental data.

It turns out, from Eq. (4.1), that $\dot{\sigma}_\infty \Phi^{-2}$ is the flow rate independent constant c. In Fig. 7, the plots of $\dot{\sigma}(x)\Phi^{-2}$ for the several flow rate cases corroborates, in fact, the predicted collapse of data for larger values of the measurement position x. The horizontal solid line in Fig. 7 follows from the asymptotic mass deposition rate, $\dot{\sigma}_\infty = c\Phi^2$, where the numerical value of c is taken from the previous analysis for the flow rate case $\Phi = 300$ l/h, as described for Fig. 6.

In Fig. 8, we show individual fittings of the measured mass deposition rates by the use of Eq. (3.14). The matching between analytical and experimental results is still very satisfactory. We take $\alpha = 0$, while b and c have the same values as the ones reported in the description of Fig. 6, and a is the only free parameter for data fitting (obtained, again, from discarding the first three points from left to right in each dataset). We get, in units of g/m·h, $a \times 2\pi R = 19.3$ for $\Phi = 450$ l/h; $a \times 2\pi R = 21.8$ for $\Phi = 600$ l/h; $a \times 2\pi R = 25.5$ for $\Phi = 750$ l/h. Due to the much larger error bars for the flow rate case $\Phi = 1000$ l/h, we did not attempt to determine its associated value of a; therefore, we just plot, for this instance, the horizontal line associated to the asymptotic mass deposition rate $\dot{\sigma} = c\Phi^2$. The error bars in Fig. 8 were estimated from the specific number of independent experimental runs for each flow rate case: three runs for $\Phi = 450$ l/h; five runs for $\Phi = 600$ l/h; six runs for $\Phi = 750$ l/h; two runs for $\Phi = 1000$ l/h.

To conclude the present analysis, we drive our attention to the regime of ion-by-ion limescale formation which is observed closer to the pipe's inlet. As stated in Eqs. (3.2) and (3.14) (with $\alpha = 0$), the mass deposition rates are expected to crossover from a linear to a quadratic dependence on the flow rate, as measurement positions get farther away from the pipe's inlet. This piece of information is, actually, a useful clue to establish an extended collapse of data for the measured mass deposition rates. An educated guess is to introduce an interpolating scaling exponent $\zeta = \zeta(x)$, such that $\dot{\sigma}(x) \propto \Phi^{\zeta(x)}$, where $\zeta(x) = 1$ at the pipe's inlet and $\zeta(x) = 2$ at the pipe's outlet. Out of an infinity of possible interpolations, the simplest choice, the linear one, is found to yield a suggestive data collapse of the measured mass deposition rates for all of the investigated flow rate cases, as it can be clearly seen from Fig. 9. More concretely, the mass deposition rates are normalized in Fig. 9 by a "sliding" power of the flow rate, that is, Φ^ζ with $\zeta = 1.0 + (i-1)/11$, where $i = 1, 2, \ldots, 12$ labels the sequence of measurement points. Results are reported there in monolog scale, since $\dot{\sigma}(x)\Phi^{-\zeta(x)}$ changes by a factor of 10^3 as x varies along the entire pipe's extension.

It is clear that the existence of a global data collapse like the one shown in Fig. 9 has great potential for practical applications. The issue of dynamical similarity, which is out of the scope of this work, calls for additional investigations. Relevant dimensional quantities such as ion concentrations, the friction velocity, the pipe's radius, etc. should be varied in experimental test matrices to establish useful scale-independent (that is, dimensionless) mass deposition rates. Only in this way limescale formation in industrial pipe flows could be predicted from the results of experimental tests performed at the scales of laboratory facilities.

5. Conclusions and outlook

We have compiled, for the sake of model building, a number of phenomenological features of limescale formation in turbulent pipe flows. The microscopic characterization of the calcium carbonate scale, flow-induced pipe roughness, and particle size distributions were directly obtained from our experiments. Further important inputs came from current ideas on turbophoresis phenomenology.

The top-down modeling strategy we have adopted places emphasis on general aspects of limescale formation and should eventually match results derived from the study of the detailed coupling between hydrodynamic phenomena and the chemical processes of particle nucleation and aggregation. It is reasonable to assume, from a heuristic point of view, that top-down and the more complex bottom-top approaches, like the one addressed in Kostoglou and Karabelas [33], are absolutely fundamental to achieve progress in the understanding of limescale formation in the presence of turbulence flows.

The picture that emerges from our analyses is that both ion-by-ion and particulate deposition take place in large scale turbulent pipe flow experiments where the ionic solutions are mixed right at the pipe's inlet. We have been able to devise modeling expressions for the mass deposition rates related to those two distinct physical pictures, which

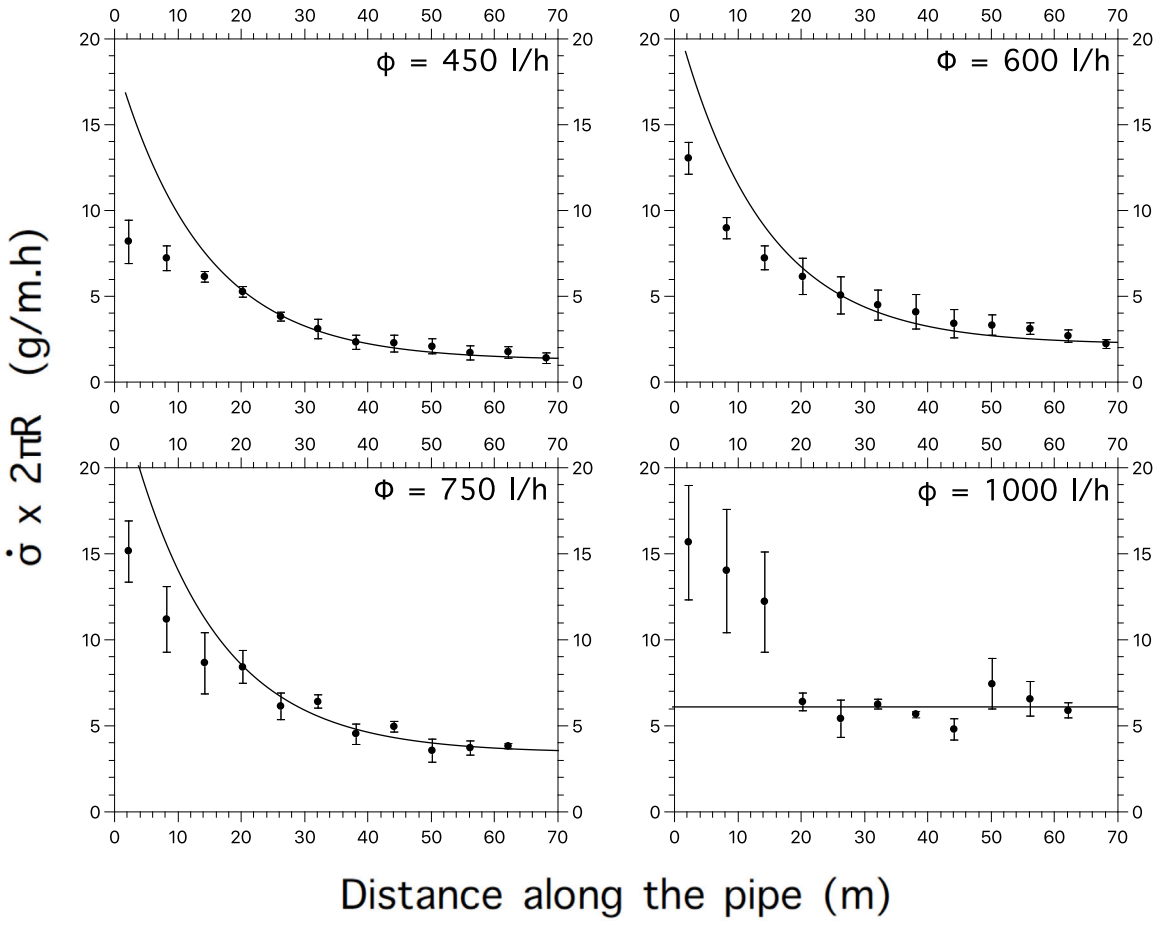

Fig. 8. Measured and modeled mass deposition rates for the flow rate cases besides $\Phi = 300$ l/h.

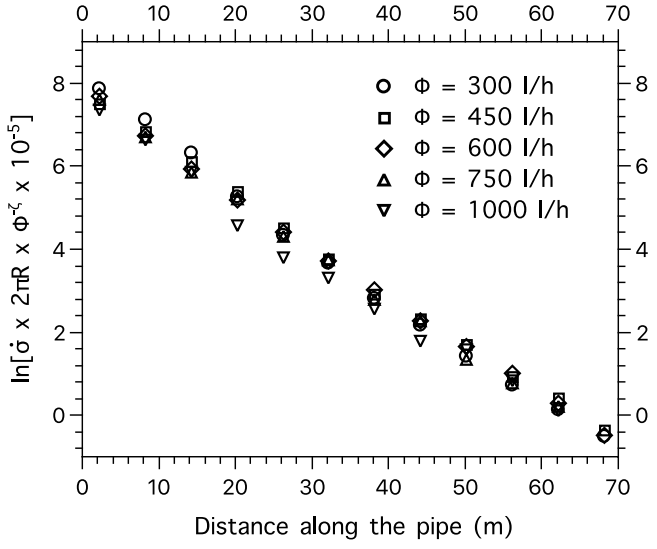

Fig. 9. Full data collapse for all of the measured mass deposition rates.

are well supported by measurements. Our main result, in short words, is the prediction that the mass deposition rate scales as

$$\dot{\sigma} \propto \frac{\Phi^{\alpha}}{R^{\beta}}, \tag{5.1}$$

with $\alpha = 1$ and $\beta = 2$ for the case of ion-by-ion deposition, while $\alpha = 2$ and $\beta = 5$ are the scaling exponents predicted for the regime of particulate deposition. Data collapse, as illustrated in Figs. 7 and 9, points out that a dynamic similarity theory of limescale formation is a promising perspective in the research horizon of particle-laden flows.

Much further work is in order. As an immediate task, it would be important to address the role of chemical concentrations and thermodynamic conditions in the behavior of the mechanical kinetic constants (3.15), (3.16), and (3.17). Determinations of the scaling exponent β described in (5.1) are also still completely open for experimental validation.

As main modeling restrictions, it is important to note that the present model has its domain of applicability limited to the case of approximately Newtonian fluids and dilute particle suspensions (so that particle aggregation takes place through binary collisions). Also, we emphasize that the asymptotic result given by Eq. (4.1) is assumed to hold only for the (usual) situations where the transported mass flow rate along the pipe is much larger than the mass deposition rate per unit area.

Moving towards a deeper level of modeling, one would be interested to clarify the detailed mechanisms for the adhesion of the smaller calcium carbonate particles snapshotted in Figs. 2c and 2d, and the puzzlingly way how they are brought to the pipe's surface, as discussed in Section 3. A plausible solution of this problem could be based on the (well reported) aggregation of metastable small vaterite globules, bonded into larger clusters [34,35], which would then behave as inertial particles in the turbulent boundary layer.

CRediT authorship contribution statement

L. Moriconi: Conceptualization, Methodology, Software, Formal analysis, Investigation, Writing – original draft, Writing – review &

editing, Visualization. **T. Nascimento:** Software, Validation, Investigation, Data curation. **B.G.B. de Souza:** Software, Validation, Investigation, Data curation. **J.B.R. Loureiro:** Conceptualization, Software, Investigation, Resources, Supervision, Project administration, Funding acquisition.

Declaration of competing interest

The authors declare that they have no known competing financial interests or personal relationships that could have appeared to influence the work reported in this paper.

Acknowledgments

The authors thank A. Barreto, E. Dittrich, D. Naiff, G. Pires, and F. Ramos for enlightening discussions. This work has been partially supported by the Conselho Nacional de Desenvolvimento Científico e Tecnológico (CNPq), Brazil, Coordenação de Aperfeiçoamento de Pessoal de Nível Superior (CAPES), Brazil and Petrobras (COPPETEC project number 20459).

Appendix. Sizes of surface-adhering particles

Instead of digging into very specific details of the DLVO theory of microscopic particle–particle or particle–surface interactions [36], our aim, in this appendix, is just to get "back of envelope" estimates for the sizes of calcium carbonate particles that can be deposited in wall-bounded turbulence. In contrast with electrochemical discussions which are carried out in equilibrium contexts, the following arguments take into account relevant dynamic properties of boundary layer flows. As a simplification, we focus our attention on calcium carbonate particles and surfaces which are electrically neutral.

To start, consider a spherical particle of radius R_p which stands in the vicinity of a planar material surface. Let y be the distance between the material plane and the closest point on the particle's surface. The attractive van der Waals force between the particle and the surface can be written as [36]

$$F_W(y) = \frac{AR_p}{6y^2} \ , \tag{A.1}$$

where A is the so-called Hamaker constant,

$$A = \pi^2 C n_1 n_2 \ , \tag{A.2}$$

and n_1 and n_2 represent the molecular number densities of the particle and the surface, while C is a medium-dependent constant. For water, typically,

$$C \simeq 1.4 \times 10^{-77} \ \mathrm{J \cdot m^6} \ . \tag{A.3}$$

The whole point here is to understand whether a neutral spherical particle will be captured by the surface when transported by a turbulent flow. We expect to have particle adhesion if

(i) $F_W(y) > F_D = 6\pi\mu R_p v$, that is, if van der Waals forces overcome Stokes drag for the situation where μ is the dynamic viscosity of water and v is the fluid velocity in the lab's reference frame;

(ii) $\frac{1}{2}mv^2 < \int_y^\infty dx F_W(x) = AR_p/6y$, that is, if a particle has enough kinetic energy to escape from the surface, once its departing (wall-normal) velocity at distance y is v.

Conditions (i) and (ii) can be reshuffled, respectively, as

(i') $f_1(y) \equiv A/(36\pi y^2 \mu v) > 1$ and (ii') $f_2(y) \equiv A/(4\rho_p R_p^2 y v^2) > 1$.

As a case study, we consider a pipe flow in its initial stages of limescale formation, such that surface roughness can be neglected, with $\mathrm{Re} = 2 \times 10^4$ (flow rate of $\simeq 600$ l/h in our experiments). The related friction Reynolds number is $R_\tau = 576$ and the friction velocity is, accordingly, $v_* = \nu R_\tau / R \simeq 0.1$ m/s. The calcium carbonate molecular number density and its mass density are, respectively, $n = 2.7 \times 10^{27}/\mathrm{m}^3$ and $\rho_p = 2.7 \times 10^3$ Kg/m^3. For the interaction of calcium carbonate species, the Hamaker constant is evaluated, from (A.2) and (A.3), as $A \simeq 1.1 \times 10^{-20}$ J.

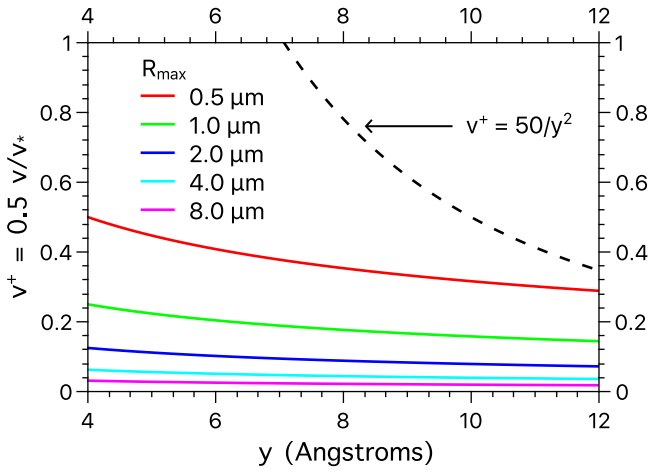

Fig. 10. Values of R_{max} for the flow rate case $\Phi = 600$ l/h with $\mathrm{Re} \simeq 2 \times 10^4$. (For interpretation of the references to color in this figure legend, the reader is referred to the web version of this article.)

For a particle with departing dimensionless velocity defined, for convenience, as $v^+ \equiv 0.5 v/v_*$ at a distance y, in Angstroms, from the attracting surface, condition (ii') leads to the maximum particle radius for deposition,

$$R_{max} \simeq \sqrt{\frac{1}{y(v^+)^2}} \ \mu\mathrm{m} \ . \tag{A.4}$$

Condition (i'), on its turn, gives

$$v^+ < \frac{50}{y^2} \ . \tag{A.5}$$

We get, from Fig. 10, graphic information on the values of R_{max} associated to physically meaningful ranges of y and v^+ in a turbulent boundary layer. The colored curves in Fig. 10 indicate, for each pair of parameters, (v^+, y), the values of maximum particle radius for electric capture (van der Waals) by the surface. Particle adhesion does not occur if (v^+, y) lies above the dashed line. This analysis suggests that transported neutral calcium carbonate particles can be deposited only if they have at most sizes of a few micrometers, in qualitative agreement with the SEM images reported in Figs. 2c and 2d.

References

[1] P.G. Koutsoukos, C.G. Kontoyannis, Precipitation of calcium carbonate in aqueous solutions, J. Chem. Soc. Faraday Trans. 1 80 (1984) 1181, http://dx.doi.org/10.1039/F19848001181.

[2] L. Lin, W. Jiang, X. Xu, P. Xu, A critical review of the application of electromagnetic fields for scaling control in water systems: mechanisms, characterization, and operation, NPJ Clean Water 3 (2020) 25, http://dx.doi.org/10.1038/s41545-020-0071-9.

[3] O.J. Vetter, W.A. Farone, Calcium Carbonate Scale in Oilfield Operations, in: Paper presented at the SPE Annual Technical Conference and Exhibition, Dallas, Texas, 1987, https://doi.org/10.2118/16908-MS.

[4] A. Neville, Surface scaling in the oil and gas sector: Understanding the process and means of management, Energy Fuels 26 (2012) 4158, http://dx.doi.org/10.1021/ef300351w.

[5] A.A. Olajire, A review of oilfield scale management technology for oil and gas production, J. Petrol. Sci. Eng. 135 (2015) 723, http://dx.doi.org/10.1016/j.petrol.2015.09.011.

[6] T.P. Burchette, Carbonate rocks and petroleum reservoirs: A geological perspective from the industry, Geol. Soc. Spec. Publ. 370 (2012) 17, http://dx.doi.org/10.1144/SP370.14.

[7] M. Broby, M. Neteland, X. Ma, J.-P. Andreassen, M. Seiersten, Scaling of Calcium Carbonate on Heated Surfaces - Crystallization or Particulate Fouling? in: the Proc. of the SPE International Oilfield Scale Conference and Exhibition, Aberdeen, Scotland, UK, 2016, https://doi.org/10.2118/179901-MS.

[8] O. Bello, Calcium Carbonate Scale Deposition Kinetics on Stainless Steel Surfaces PhD Dissertation, The University of Leeds, 2017, https://etheses.whiterose.ac.uk/17647/.
[9] MacAdam, S.A. Parsons, Calcium carbonate scale formation and control, Rev. Environ. Sci. Biotechnol. 3 (2004) 159, http://dx.doi.org/10.1007/s11157-004-3849-1.
[10] S. Kumar, T.K. Naiya, T. Kumar, Developments in oilfield scale handling towards green technology-a review, J. Petrol. Sci. Eng. 169 (2018) 428, http://dx.doi.org/10.1016/j.petrol.2018.05.068.
[11] M.A.J. Mazumder, A review of green scale inhibitors: Process, types, mechanism and properties, Coatings 10 (2020) 928, http://dx.doi.org/10.3390/coatings10100928.
[12] D. Gebauer, A. Völkel, H. Cölfen, Stable prenucleation calcium carbonate clusters, Science 322 (2008) 1819, http://dx.doi.org/10.1126/science.1164271.
[13] A.F. Wallace, L.O. Hedges, A. Fernandez-Martinez, P. Raiteri, J.D. Gale, G.A. Waychunas, S. Whitelam, J.F. Banfield, J.J. De Yoreo, Microscopic evidence for liquid-liquid separation in supersaturated $CaCO_3$ solutions, Science 341 (2013) 885, http://dx.doi.org/10.1126/science.1230915.
[14] M.H. Nielsen, S. Aloni, J.J. De Yoreo, In situ TEM imaging of $CaCO_3$ nucleation reveals coexistence of direct and indirect pathways, Science 345 (2014) 1158, http://dx.doi.org/10.1126/science.1254051.
[15] A. Koishi, Carbonate Mineral Nucleation Pathways, UniversitÉ Grenoble Alpes, (Ph.D. thesis), 2017, https://tel.archives-ouvertes.fr/tel-01701947/document.
[16] A. Carino, A. Testino, M.R. Andalibi, F. Pilger, P. Bowen, C. Ludwig, Thermodynamic-kinetic precipitation modeling. a case study: The amorphous calcium carbonate (ACC) precipitation pathway unravelled, Cryst. Growth Des. 17 (2017) 2006, http://dx.doi.org/10.1021/acs.cgd.7b00006.
[17] R. de P. Cosmo, F. de A.R. Pereira, D. da C. Ribeiro, W.Q. Barros, A.L. Martins, Estimating CO2 degassing effect on $CaCO_3$ precipitation under oil well conditions, J. Petrol. Sci. Eng. 81 (2019) 106207, http://dx.doi.org/10.1016/j.petrol.2019.106207.
[18] A.V.A. de Souza, F. Rosário, J. Cajaiba, Evaluation of calcium carbonate inhibitors using sintered metal filter in a pressurized dynamic system, Materials 12 (2019) 1849, http://dx.doi.org/10.3390/ma12111849.
[19] M.W. Reeks, The transport of discrete particles in inhomogeneous turbulence, J. Aerosol Sci. 14 (1983) 729, http://dx.doi.org/10.1016/0021-8502(83)90055-1.
[20] J. Young, A. Leeming, A theory of particle deposition in turbulent pipe flow, J. Fluid Mech. 340 (1997) 129, http://dx.doi.org/10.1017/S0022112097005284.
[21] C. Marchioli, A. Soldati, Mechanisms for particle transfer and segregation in a turbulent boundary layer, J. Fluid Mech. 468 (2002) 283.
[22] A. Guha, Transport and deposition of particles in turbulent and laminar flow, Annu. Rev. Fluid Mech. 40 (2008) 311, http://dx.doi.org/10.1146/annurev.fluid.40.111406.102220.
[23] F. Picano, G. Sardina, C.M. Casciola, Spatial development of particle-laden turbulent pipe flow, Phys. Fluids 21 (2009) 093305, http://dx.doi.org/10.1063/1.3241992.
[24] G. Sardina, P. Schlatter, L. Brandt, F. Picano, C.M. Casciola, Wall accumulation and spatial localization in particle-laden wall flows, J. Fluid Mech. 699 (2012) 50, http://dx.doi.org/10.1017/jfm.2012.65.
[25] W.K. Burton, N. Cabrera, F.C. Frank, The growth of crystals and the equilibrium structure of their surfaces, Phil. Trans. R. Soc. A 243 (1951) 299, http://dx.doi.org/10.1098/rsta.1951.0006.
[26] T.A. Witten, L.M. Sander, Diffusion-limited aggregation, Phys. Rev. B 27 (1983) 5686, http://dx.doi.org/10.1103/PhysRevB.27.5686.
[27] Y.A. Çengel e J.M. Cimbal, Fluid Mechanics, McGraw-Hill, 2006.
[28] S.B. Pope, Turbulent Flows, Cambridge University Press, 2000.
[29] A.-L. Barabasi, H.E. Stanley, Fractal Concepts in Surface Growth, Cambridge University Press, 1995.
[30] The reference Stokes number $St^+ \simeq 5$ should not be taken in a very rigorous sense; it is, rather, an approximation, which we use to get particle sizes estimates. Actually, we expect turbophoresis effects to be relevant in the deposition processes for $St^+ = O(1)$. Threshold values of the Stokes number can also depend on surface roughness.
[31] Y. Cao, M. Xin, Numerical simulation of supercooled large droplet icing phenomenon: A review, arch, Comput. Methods Eng. 27 (2020) 1231, http://dx.doi.org/10.1007/s11831-019-09349-5.
[32] D. Ramkrishna, Population Balances: Theory and Applications To Particulate Systems in Engineering, Academic Press, 2000.
[33] M. Kostoglou, A.J. Karabelas, Comprehensive modeling of precipitation and fouling in turbulent pipe flow, Ind. Eng. Chem. Res. 37 (1998) 1536, http://dx.doi.org/10.1021/ie970559g.
[34] J. Rieger, T. Frechen, G. Cox, W. Heckmann, C. Schmidt, J. Thieme, Precursor structures in the crystallization/precipitation processes of $CaCO_3$ and control of particle formation by polyelectrolytes, Faraday Discuss. 136 (2007) 265, http://dx.doi.org/10.1039/B701450C.
[35] Q. Hu, J. Zhang, H. Teng, U. Becker, Growth process and crystallographic properties of ammonia-induced vaterite, Am. Mineral. 97 (2012) 1437, http://dx.doi.org/10.2138/am.2012.3983.
[36] J.N. Israelachvili, Intermolecular and Surface Forces, Academic Press Limited, 1998.